

BIOHYBRID ROBOTS

Optogenetic neuromuscular actuation of a miniature electronic biohybrid robot

Hyegi Min^{1†}, Yue Wang^{2,3†}, Jiaojiao Wang^{1,4†}, Xiuyuan Li^{5,6†}, Woong Kim¹, Onur Aydin⁷, Sehong Kang⁸, Jae-Sung You^{1,4,9}, Jongwon Lim^{1,4}, Katy Wolhaupter^{1,4}, Yikang Xu¹, Zhengguang Zhu^{2,10}, Jianyu Gu², Xinming Li^{2,3}, Yongdeok Kim^{1,11}, Tarun Rao⁴, Hyun Joon Kong^{7,12,13}, Taher A. Saif^{7,8}, Yonggang Huang^{2,5,14,15*}, John A. Rogers^{2,3,14,15,16,17*}, Rashid Bashir^{1,4,7,13,18*}

Copyright © 2025 The Authors, some rights reserved; exclusive licensee American Association for the Advancement of Science. No claim to original U.S. Government Works

Neuronal control of skeletal muscle function is ubiquitous across species for locomotion and doing work. In particular, emergent behaviors of neurons in biohybrid neuromuscular systems can advance bioinspired locomotion research. Although recent studies have demonstrated that chemical or optogenetic stimulation of neurons can control muscular actuation through the neuromuscular junction (NMJ), the correlation between neuronal activities and resulting modulation in the muscle responses is less understood, hindering the engineering of high-level functional biohybrid systems. Here, we developed NMJ-based biohybrid crawling robots with optogenetic mouse motor neurons, skeletal muscles, 3D-printed hydrogel scaffolds, and integrated onboard wireless micro-light-emitting diode (μ LED)-based optoelectronics. We investigated the coupling of the light stimulation and neuromuscular actuation through power spectral density (PSD) analysis. We verified the modulation of the mechanical functionality of the robot depending on the frequency of the optical stimulation to the neural tissue. We demonstrated continued muscle contraction up to 20 minutes after a 1-minute-long pulsed 2-hertz optical stimulation of the neural tissue. Furthermore, the robots were shown to maintain their mechanical functionality for more than 2 weeks. This study provides insights into reliable neuronal control with optoelectronics, supporting advancements in neuronal modulation, biohybrid intelligence, and automation.

INTRODUCTION

The central nervous system plays a critical role in controlling bodily functions, such as sensing, memory, and behavior, by transmitting neurotransmitters through synaptic communication (1). Specifically,

neuron-innervated skeletal muscles generate a range of mechanical outputs through neuromuscular junctions (NMJs). Therefore, there is growing interest in biomimicking the neuron-muscle interactions, particularly in biohybrid robotics. Thus far, actuating muscle tissues integrated with two- or three-dimensional (3D) scaffolds have been developed to mimic bodily movements like swimming (2–4), walking (5–9), and grabbing (10). Although some studies have used electrical stimulation to activate voltage-gated ion channels (8, 9, 11, 12), others have used optical stimulation on optogenetically transduced myotubes for spatial control of actuation (4, 7, 13). Biological stimulation through motor units, which can autonomously maintain firing and act as biobatteries or oscillators, holds potential for next-generation biohybrid robots. However, autonomous functions through neuromuscular units remain underexplored, with only a few demonstrations to date (2, 5). Although chemical excitation and inhibition of pre- and postsynaptic areas (2, 5, 14, 15) and electromechanical stimulation of NMJ gap junctions have been demonstrated inducing direct stimulation on neurons (9), a deeper demonstration and understanding of the modulation and automation of neural activity remain challenging, especially as these relate to creation of high-level biomimetic systems.

A key method for modulating neural activity involves exposing neurons to external stimulation to evoke neuronal firing. One of the approaches uses optogenetic control by introducing light-gated ion channels, such as channelrhodopsin-2 (ChR2), into the neurons (16) and has proven particularly useful in neuroscience. For example, optogenetic stimulation of the motor cortex in monkeys has induced forelimb movements (17), whereas in mice, optogenetic motor neurons have been used to restore muscle function by reinnervating damaged muscles (18). Optical stimulation of ventral tegmental area (VTA) dopaminergic neurons has also been shown

¹Nick J. Holonyak Micro and Nanotechnology Laboratory, Grainger College of Engineering, University of Illinois at Urbana-Champaign, Urbana, IL 61801, USA. ²Querrey Simpson Institute for Bioelectronics, Northwestern University, Evanston, IL 60208, USA. ³Department of Biomedical Engineering, Northwestern University, Evanston, IL 60208, USA. ⁴Department of Bioengineering, Grainger College of Engineering, University of Illinois at Urbana-Champaign, Urbana, IL 61801, USA. ⁵Department of Civil and Environmental Engineering, Northwestern University, Evanston, IL 60208, USA. ⁶State Key Laboratory of Mechanical System and Vibration, School of Mechanical Engineering, Shanghai Jiao Tong University, Shanghai 200240, China. ⁷Scott H. Fisher Multi-Cellular Engineered Living System Theme, Carl R. Woese Institute for Genomic Biology, University of Illinois at Urbana-Champaign, Urbana, IL 61801, USA. ⁸Department of Mechanical Science and Engineering, Grainger College of Engineering, University of Illinois at Urbana-Champaign, Urbana, IL 61801, USA. ⁹Department of Cell and Developmental Biology, Grainger College of Engineering, University of Illinois at Urbana-Champaign, Urbana, IL, USA. ¹⁰Department of Chemical and Biological Engineering, Northwestern University, Evanston, IL 60208, USA. ¹¹Department of Materials Science and Engineering, Grainger College of Engineering, University of Illinois at Urbana-Champaign, Urbana, IL, USA. ¹²Department of Chemical and Biomolecular Engineering, Grainger College of Engineering, University of Illinois at Urbana-Champaign, Urbana, IL 61801, USA. ¹³Chan Zuckerberg Biohub Chicago, Chicago, IL 60642, USA. ¹⁴Department of Materials Science and Engineering, Northwestern University, Evanston, IL 60208, USA. ¹⁵Department of Mechanical Engineering, Northwestern University, Evanston, IL 60208, USA. ¹⁶Department of Neurological Surgery, Feinberg School of Medicine, Northwestern University, Chicago, IL 60611, USA. ¹⁷Center for Bio-Integrated Electronics, Northwestern University, Evanston, IL 60208, USA. ¹⁸Department of Biomedical and Translational Sciences, Carle Illinois College of Medicine, Urbana, IL 61801, USA.

*Corresponding author. Email: y-huang@northwestern.edu (Y.H.); jrogers@northwestern.edu (J.A.R.); rbashir@illinois.edu (R.B.)

†These authors contributed equally to this work.

to release dopamine (19), detectable by electrochemical sensors. Some studies have reported emergent behaviors in neural networks, such as synchronicity, oscillation, plasticity, and self-organization. For example, engineered neural tissue (NT) models have demonstrated synchronized activity of the entire tissue using spot stimulation (20). Repetitive line-scanning optical stimulation of optogenetic NT has been shown to encode neuronal plasticity pathways (21). These signaling processes have gained substantial interest from researchers seeking to mimic the “emergent behaviors” of neurons through training with external stimuli. Neurons have also been shown to adapt to unpredictable stimulus conditions by minimizing their internal free energy, holding promise for developing neurorehabilitation (22), gaming (23), and neuronal computing systems (24). Although these studies have made notable progress in modulating functional outputs via neuronal activity, the neuronal-to-mechanical transduction remains less understood.

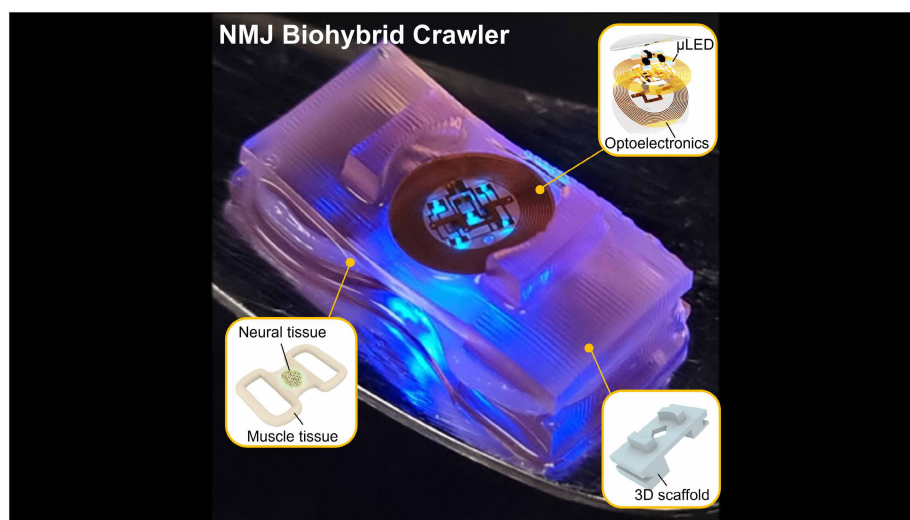
In this study, we aimed to address these questions by developing a robust *in vitro* NMJ-driven biohybrid crawling system that combines optogenetic motor neurons with skeletal muscles on a 3D-printed hydrogel scaffold with wireless onboard optoelectronics (Movie 1 and Fig. 1A). We demonstrated single- and dual-NT NMJ biohybrid crawlers by varying scaffold designs, resulting in crawling driven by spontaneous or stimulated neuronal firing. Finite element analysis (FEA) supported our experimental observations, revealing mechanistic insights into the locomotive behavior. Using wireless-controlled onboard electronics, we delivered light pulses with varying frequencies to modulate neuronal activity resulting in dynamic actuation of the skeletal muscle tissue and resulting motion. We analyzed both autonomous and stimulated actuation behaviors in the crawler through power spectral density (PSD) analysis to investigate the correlation between mechanical output and modulated neuronal activity. The integration of micro-light-emitting diodes (μ LEDs) with NMJ crawlers enabled reliable optogenetic stimulation and facilitated a detailed understanding of the mechanical outputs of skeletal muscle driven by neuronal inputs. These findings offer a valuable perspective on neural tuning and its role in modulating skeletal muscle outputs, paving the way for developing advanced biohybrid robotics capable of adaptive learning and enhancing our understanding of neuromuscular activities.

RESULTS

Formation of the 3D neuromuscular tissue on a synthetic scaffold

The overall experimental procedures are illustrated in Fig. 1B. A 3D two-legged skeleton scaffold with dimensions of 7 mm by 14 mm by 3.6 mm was fabricated using stereolithography with polyethylene glycol diacrylate [PEGDA; number-average molecular weight (M_n) \sim 700 g/mol], designed to demonstrate unidirectional crawling behavior. According to dynamic mechanical analysis (DMA) (25), the Young's modulus of the printed hydrogel structure was \sim 250 kPa. To directly integrate a muscle tissue into the skeleton, we prepared an additional mold as described in the previous mold injection method (13). We also designed an insertable pole structure to create a through-hole in the muscle tissue, where neurospheres would later be seeded for the single-NT system (fig. S1). After assembling these parts, C2C12 mouse skeletal myoblasts were seeded into the mold with Matrigel and fibrin. After tissue seeding, the myoblasts continued to proliferate in the growth medium (GM), compacting for 3 days in the presence of 6-aminocaproic acid (ACA) to inhibit degradation of fibrin by enzymes (7). The samples were then cultured in the muscle differentiation medium (DM) for 5 days to facilitate the formation of contractile myotubes. Neurospheres containing optogenetic motor neurons were derived separately by directed differentiation of optogenetic mouse embryonic stem cells (mESCs) toward lower spinal cord motor neurons following established protocols (26–28). The insert pole at the center of the muscle tissue was removed, and the neurospheres were transplanted into the resulting cavity in a fibrin-Matrigel mixture to initiate coculture. We also designed a dual-NT model to evaluate the functionality of NMJs and the motility of crawlers on the basis of the location of NTs (fig. S2). For this, two chambers were created, one at the center of each leg. Similar to the single-NT NMJ system, insertion structures were added to the chamber before seeding myoblasts to occupy spaces for neurospheres. These chambers featured inward-facing slits, a series of posts (50 μ m) and gaps (100 μ m), to stably anchor the muscle tissue close to the neural matrix and provide pathways for the extension of neurites and formation of NMJs. Figure 1C shows images of both single- and dual-NT NMJ biohybrid crawlers, displaying the neurospheres alongside the muscle strip.

Neurospheres were imaged using bright-field and fluorescence microscopy to characterize their morphology and phenotype (Fig. 1D). Bright-field imaging showed that the overall size of spheroids was $189.17 \pm 43.82 \mu\text{m}$. The mESCs were transduced with fluorescently tagged promoters, HB9–green fluorescent protein (GFP) and ChR2–tdTomato, to visualize motor neurons and light-gated ion channels (29). Fluorescence imaging revealed ChR2–tdTomato⁺ (i.e., optogenetic) cells throughout the spheroid, a subset of which was HB9–GFP⁺ motor neurons. We also visualized the entire NMJ crawler to verify the confinement of neuronal cells in the seeding region. As shown in the phase-contrast image in Fig. 1E, both the muscle strip and the neurospheres were distinctly observed, showing close contact between them. Fluorescence images revealed GFP and tdTomato signals in the center of the



Movie 1. Overview of the NMJ-based biohybrid crawling robot.

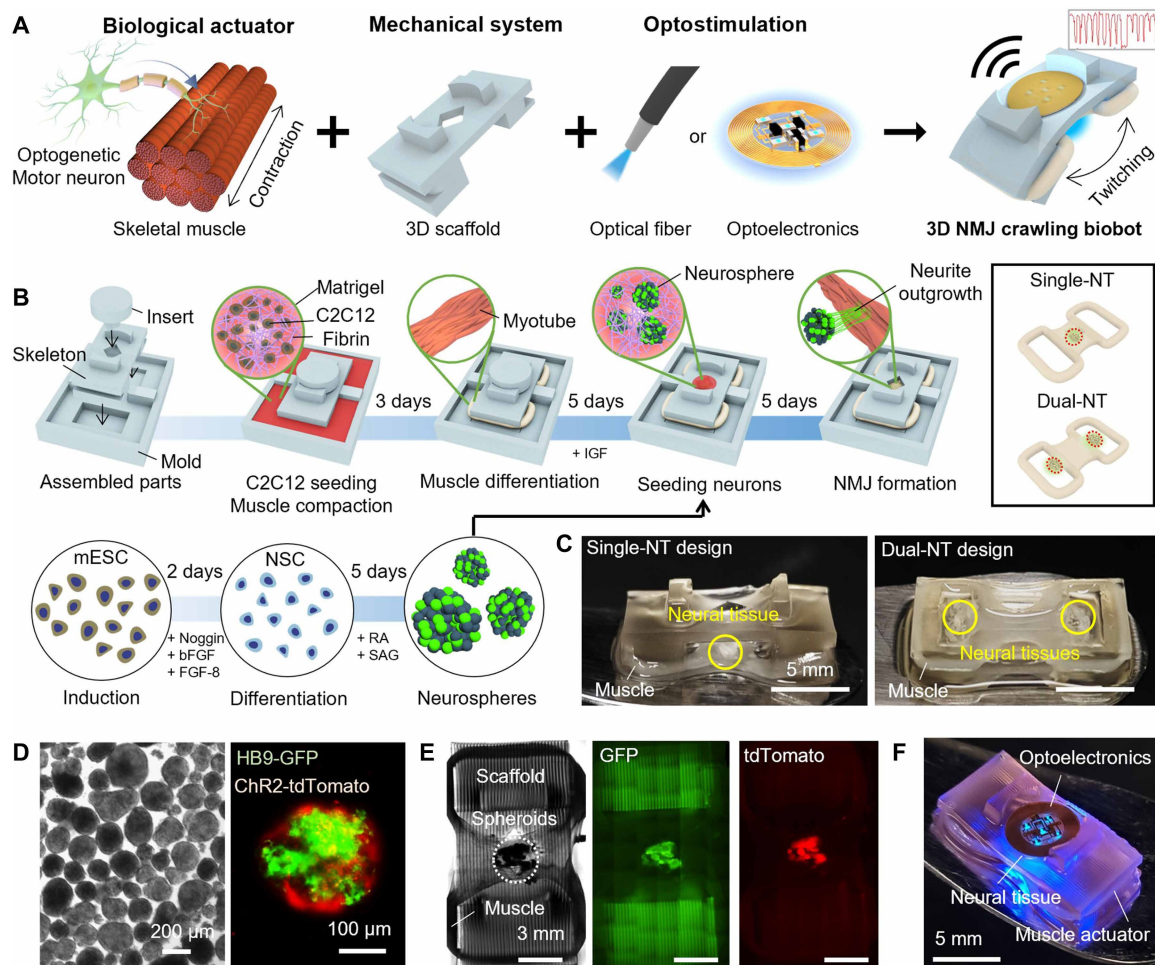


Fig. 1. Fabrication of NMJ-driven biohybrid crawler with μ LED optoelectronics. (A) Brief illustration of key components of the NMJ crawler. (B) Schematics of the experimental procedure for NMJ tissue preparation. Depending on where neural chambers exist, NTs are located at the center of or beside the muscle tissue. Inset shows the two versions of NMJ models, single-NT and dual-NT. Red dotted circle denotes boundary of NTs that form the NMJ in a lateral direction. (C) Pictures of single- and dual-NT NMJ crawlers. Scale bars, 5 mm. (D) Fluorescence expression of optogenetic mESCs transduced by HB9-GFP and ChR2-tdTomato. Scale bars, 200 and 100 μ m. (E) Fluorescence mapping of a whole NMJ crawler showing the localization of neurospheres in the tissue. Scale bars, 3 mm. (F) Representative image of the completely integrated NMJ crawler. Scale bar, 5 mm.

muscle tissue, indicating that the neurospheres stayed within the seeding region at the center of the muscle strip. Last, the optoelectronic device was integrated into the scaffold as shown in Fig. 1F to complete the assembly of the biohybrid NMJ crawler. We placed the optoelectronic device on top of the crawler, in the middle of stopper structures, to enable spatial stimulation of neurospheres. This device emitted 460-nm blue light via five μ LEDs and was powered and controlled wirelessly by resonant magnetic induction coils from an external transmitter.

Characterization of NMJs

We further investigated protein expressions and localization through immunostaining of the neuromuscular tissues (Fig. 2A). After 5 days of coculture, the single-NT neuromuscular tissues were fixed in paraformaldehyde (PFA) and bound to target myosin 4 monoclonal antibodies (MF-20), beta-III-tubulin (Tuj1), 4',6-diamidino-2-phenylindole (DAPI), and α -bungarotoxin (α -BTX) to stain myosin heavy chain, microtubules, cell nucleus, and acetylcholine receptors (AChRs),

respectively. The expression of MF-20 was observed over the entire muscle tissue, indicating differentiated myotubes expressing myosin heavy chain. At the junction interfaces, Tuj1 was brightly observed in a spherical shape, representing a body of neurospheres. We observed the extension of neurites from spheroids to muscles, potentially caused by the biological signaling for synaptogenesis via agrin and laminin (30). In addition, we detected α -BTX expression on the surface of myotubes, signifying the clustering of postsynaptic AChRs (fig. S3). These results are in accordance with previous reports of imaging neuromuscular synaptic interfaces in *in vitro* systems (fig. S4) (5, 29, 31).

Neuromuscular tissues were collected and analyzed using quantitative polymerase chain reaction (qPCR) to further understand genetic regulations induced by the neuromuscular interactions. Given that the most notable activity of the NMJ is synaptic communication, we examined genes related to AChR clustering and stabilization, including *MuSK*, *DOK-7*, *Rapsyn*, and *CHRNA* (Fig. 2B) (32–35). Given that the junction is formed at the surface of mature myotubes, expression levels were normalized to the housekeeping

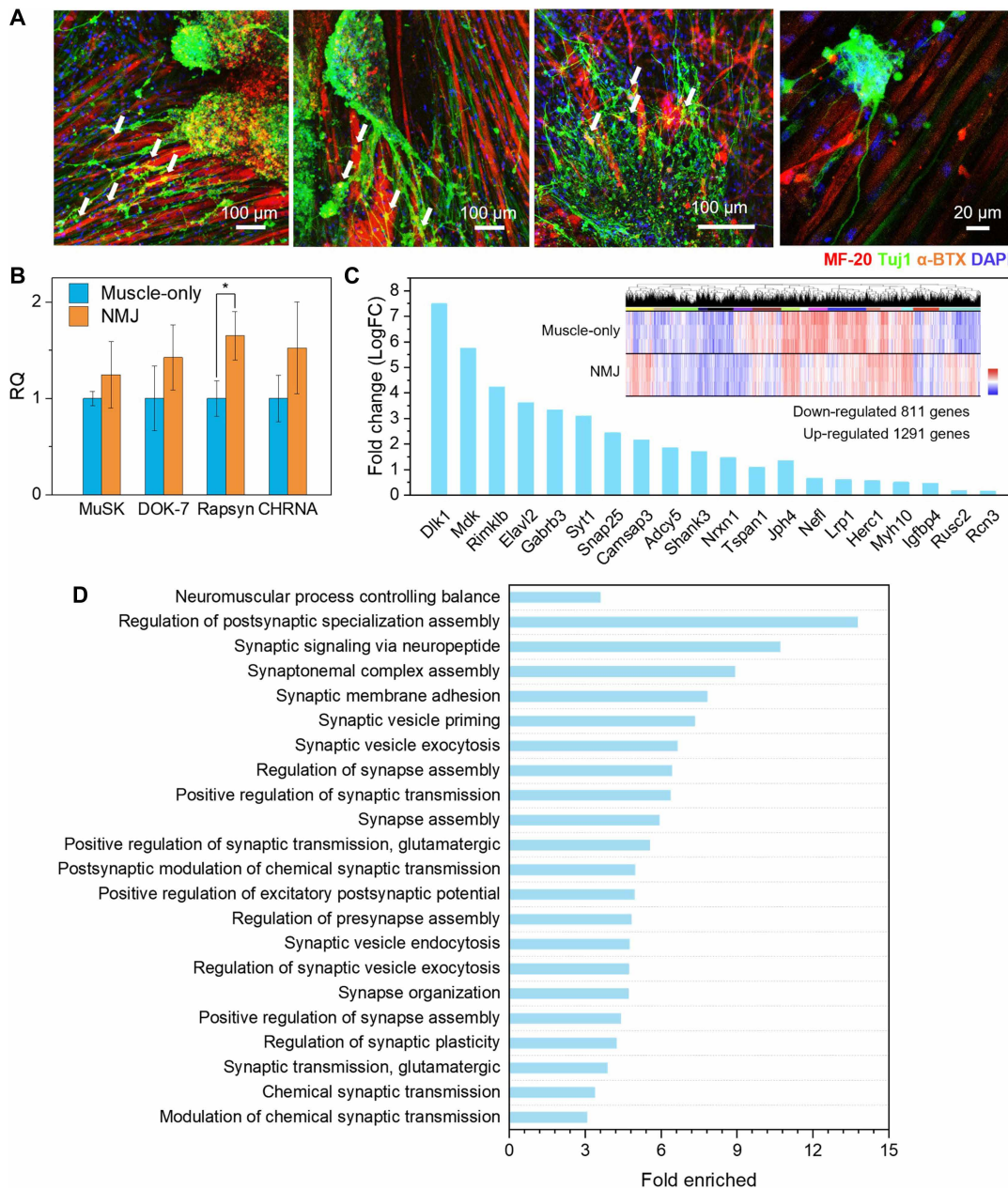


Fig. 2. Characterization of NMJs. (A) Immunostaining images of an NMJ tissue, showing myosin (MF-20, red), neuronal units (Tuj1, green), AChRs (α -BTX, orange), and cell nucleus (DAPI, blue). Scale bars, 100 and 20 μ m. White arrows denote the representative location of synaptic junctions. (B) Relative quantification (RQ) of NMJ-related genes functioning on development and stabilization of AChRs. In comparison with a muscle-only control group, neuromuscular tissues showed up-regulation of MuSK, DOK-7, Rapsyn, and CHRNA. Data represent means \pm SD ($N = 3$ biological replicates; $*P < 0.05$). (C) Analysis of the fold change of RNA expression between muscle-only and neuromuscular tissues. Inset shows the heatmap of up/down-regulated genes under a q value of 0.05 ($N = 3$ biological replicates). (D) Biological gene ontology analysis based on differentially expressed genes (FDR < 0.05).

gene and muscle creatine kinase (*MCK*) indicative of terminal muscle differentiation (36). Compared with muscle-only control groups, the relative quantity of all four genes (*MuSK*, *DOK-7*, *Rapsyn*, and *CHRNA*) appeared to be up-regulated, 1.24, 1.42, 1.65, and 1.53 times higher in the neuromuscular tissue, respectively, implying that the formation of AChR clustering was induced by the neurospheres ($N = 3$ biological replicates; $*P < 0.05$). However, there seemed to be no notable differences between muscle-only and NMJ groups, presumably because of the large differences in the muscle

and neuronal cell density, with localization and regulation of those genes at only motor endplates (37). We further verified the formation of the NMJs by investigating differentially expressed genes by mRNA sequencing (Fig. 2C). The sequencing results showed a total of 2102 genes that were differentially expressed; specifically, 811 were down-regulated and 1291 were up-regulated with a q value of less than 0.05 ($N = 3$ biological replicates). We sorted out several genes related to synaptic functions, muscle differentiation, and neuronal activity, focusing on the up-regulated genes. *Dlk1* was significantly

up-regulated, in agreement with previous reports that neuronal cells help muscle development by fostering myogenic differentiation (38). We also noted higher expression levels in *Mdk*, *Tspan1*, and *Camsap3*, which maintain neuronal polarity with stability and promote neurodevelopment and synaptogenesis (39–41). Particularly, *Mdk* is known to induce clustering of AChRs on muscles, playing a critical role in forming NMJs (39). Up-regulation of *Rimklb* and *Lrp1* indicates synaptic development (42–45). *Gabbr3* is known to influence the AChR (46). *Nrxn1* has a function of neurotransmitter release at NMJs and synapses (47). Other genes, illustrated in Fig. 2C, are also known to help promote NMJ maturation (48), neurotransmitter release (49, 50), and signaling required to form stable NMJs (51). For further information, we conducted a biological gene ontology analysis based on up-regulated differentially expressed genes [false discovery rate (FDR) < 0.05], which showed enrichment in certain biological pathways (Fig. 2D). There are enrichments in pathways related to NMJ formation, chemical synapses, and synaptic signaling processes, directly supporting formation of an NMJ, in addition to our functional results.

We conducted calcium imaging to visualize neuronal and muscular activity through the corresponding intracellular calcium ion flux (52). Neuronal firing involves calcium influx, which can be visualized using fluorescent calcium indicators. When action potentials reach the nerve terminal, acetylcholine is released into the synaptic cleft. Acetylcholine then binds to the receptors on the post-synaptic muscle membrane, inducing downstream action potentials in the muscle cells. This leads to calcium ion flux from sarcoplasmic reticulum, causing the myosin and actin filaments to slide. Therefore, both myotube contractions and neuronal firing activity can be visualized simultaneously using calcium imaging, as shown in fig. S5 (movie S1). We observed both neuronal cells and myotubes spontaneously blinking, which indicates a flux of calcium ions occurring at those cells. We believe that the small amount of glutamate content in the medium could evoke the firing of motor neurons leading to the contraction of myotubes (31). We designated several regions of interest (ROIs) for neurons and myotubes and tracked the fluorescence signal over time. We observed calcium flux occurring at a frequency of $2.1 \pm 1.3 \text{ s}^{-1}$ at the ROIs corresponding to myotubes and $1.8 \pm 0.73 \text{ s}^{-1}$ at the ROIs corresponding to neurospheres. The difference in the frequencies of calcium spikes between muscle and neuron regions was not statistically significant. Although individual neuromuscular units could not be identified morphologically in these images, the similar frequency of calcium spikes in neurons and myotubes implies a possible coupling between spontaneous muscle contraction and neuronal firing.

Analysis of crawling dynamics of NMJ robots

After confirming spontaneous neuronal signaling and active contraction of the myotubes, we investigated mechanical outputs of skeletal muscles by tracking their contraction and actual locomotion. For this analysis, we prepared two-chamber, dual-NT NMJ crawlers by seeding neurospheres into both chambers (Fig. 3A). We observed the autonomous twitching of an NMJ crawler during co-culture, verifying the functionality of the NMJs evoked by spontaneous neuronal activity (movie S2). First, we conducted FEA to confirm the unidirectional crawling behavior driven by muscle actuation. We built a hydrogel scaffold model with dimensions identical to those of the 3D-printed scaffold. A freestanding actuating strip was formed around the scaffold to induce muscle contraction and

relaxation. Two types of contractions were generated: static contraction due to the passive tension of the muscle and dynamic contraction induced by active tension of the muscle caused by neuronal activity. The material properties were obtained from previous studies (6, 12), and the muscle contraction force was characterized by experiments. The contraction curve profile was based on actual leg deflections from one of the NMJ samples showing autonomous twitching.

FEA results confirmed the unidirectional crawling locomotion derived from the asymmetric scaffold design with the actuation rate (Fig. 3B). When only static contraction existed, the crawler stood on the floor by the heel of each leg (Fig. 3B-i). When dynamic contraction occurred, both legs moved closer. The long leg, being heavier than the short one, required a higher critical friction force to overcome to slide. Therefore, whereas the short leg reached its own critical friction force, the long leg remained stationary (Fig. 3B-ii). Upon relaxation, both legs slid simultaneously because of the higher relaxation rate, exceeding the critical force for both legs. These resulted in net displacement toward the long leg side (Fig. 3B-iii). We confirmed that both the two-chamber, dual-NT and one-chamber, single-NT crawlers exhibited unidirectional locomotion toward the long leg side (movie S3). Figure 3C shows the trace of both legs obtained from experiments and simulations, illustrating the crawling mechanism. The short leg has much higher displacement than the long leg, which agrees with the mechanism identified above: frictional differences between two legs. The trace also shows the net displacement of the crawler by repeating contraction and relaxation stages. Then, we placed the crawler on a flat surface and recorded its locomotion for 1 min. As predicted by our simulation, the crawler demonstrated continuous locomotion toward the long leg side, with slight rotation, possibly because of the nonuniform density of myotubes throughout the tissue (Fig. 3D and movie S4). The crawling velocity was calculated to be 10.5 mm/min on the basis of the net displacement (Fig. 3E). The magnified view of the crawling traces shows a stepwise profile of the displacement curve, which coincides with the crawling mechanism described in Fig. 3C. In the same batch, we observed autonomous crawling behaviors from other crawlers with variable velocities (fig. S6). One of the key factors affecting this variation could be a synchronicity of the two-NT activity. We conducted FEA simulations to compare the velocity under varying stimulation frequencies and lags in the dual-NT robots to investigate the mutual influence between two NTs (fig. S7). The results indicate that the robot achieved the highest velocity when both NTs fired at the same frequency. Other possible factors of the variability could be due to variations in cell density, innervation efficiency, and myotube differentiation status and could be challenging to completely control. Through these investigations, we successfully reproduced autonomous NMJ-driven crawling in multiple samples.

Chemical regulation of neuromuscular actuations

We further characterized NMJ-driven muscle contraction by analyzing the mechanical output response to chemical stimuli. Previous reports have shown that chemical excitation with L-glutamic acid or inhibition with tubocurarine and botulinum toxin can modulate neuromuscular contraction by binding to receptors on presynaptic or postsynaptic sites (2, 14, 15, 29). Similarly, we investigated how inhibitory molecules affect the motility of autonomous crawlers. Curare, a competitive binding molecule for the acetylcholine, was added twice to an autonomous crawler with final concentrations of

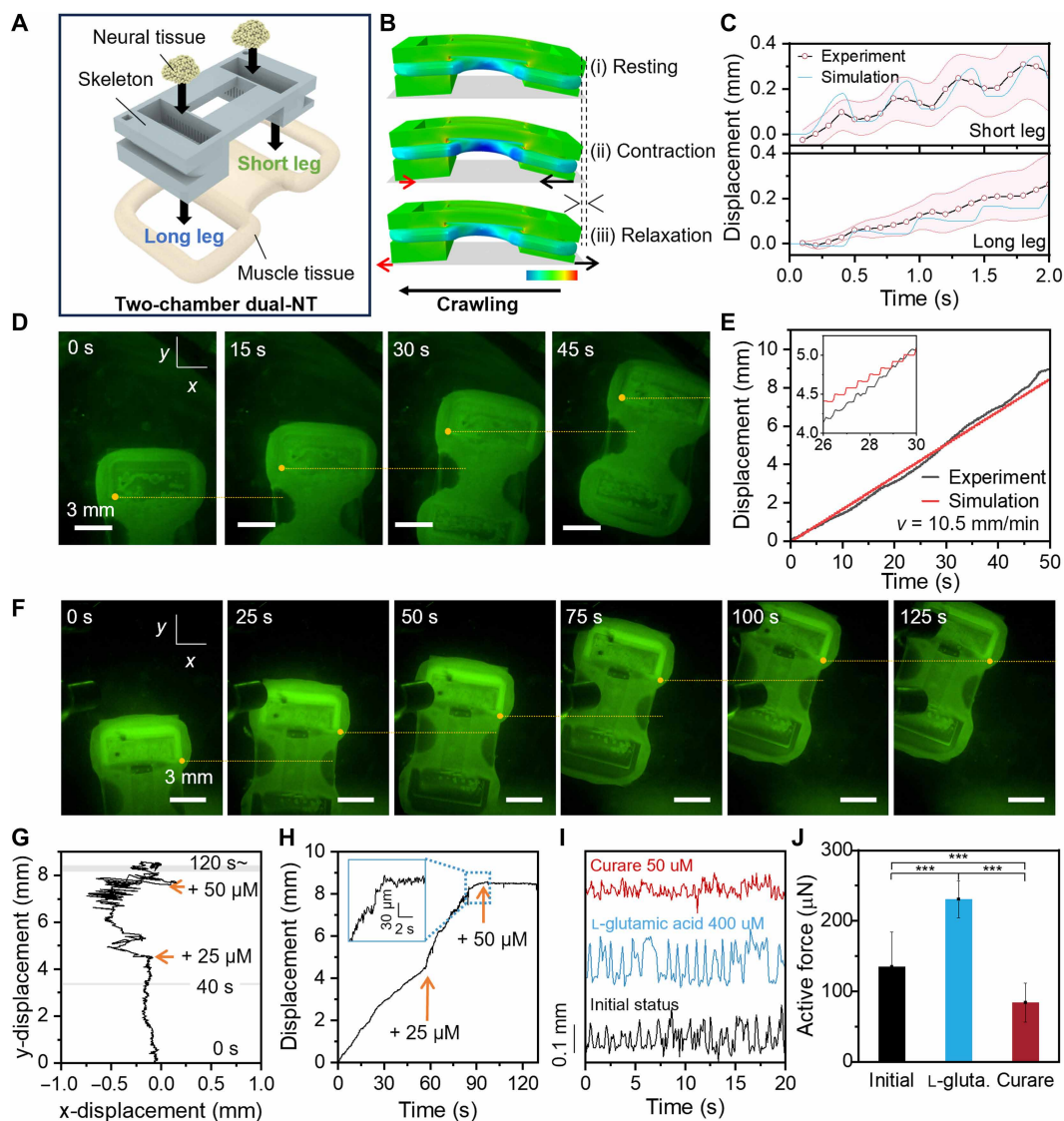


Fig. 3. Analyzing locomotion of dual-NT NMJ crawlers driven by spontaneous neuronal activity. (A) Brief illustration of a two-chamber dual-NT NMJ crawler. (B) FEA of the crawling behavior of the asymmetric scaffold. (C) Leg deflections of the long and short leg obtained from simulation (blue line) and experimental recording (black line with red circle). Data represent means \pm SD (pink-shaded area) ($N = 6$ independent trajectories). The 2.2-Hz twitching frequency was applied to the simulation. (D) Snapshots of the NMJ crawler during locomotion. Scale bars, 3 mm. (E) Comparison of crawling trajectories extracted from simulation (red) and experiment (black). (F) Chemical inhibition of crawling by adding the inhibitory molecule curare. Scale bars, 3 mm. (G) Recorded crawling trajectories in the x - y plane and (H) corresponding net displacement with increasing concentration of the curare. (I) Effect of curare and L-glutamic acid on leg deflections. (J) Statistics of contraction forces in the presence of chemicals. Data represent means \pm SD ($N = 38, 71,$ and 44 for initial status, L-glutamic acid, and curare treatment, respectively; $***P < 0.001$).

25 and 50 μM (Fig. 3F and movie S5). Although the crawler continued moving after the first addition of curare, muscle contraction slowed down and eventually stopped 30 s after the second addition. The crawling trajectory showed that the straight-line movement of the crawler was impeded after the addition of curare, denoting non-uniform or weakened contraction of the myotubes (Fig. 3G). The net displacement also indicated that the crawler remained stationary after curare was added (Fig. 3H). Considering the delayed effect of curare, sufficient time was required for diffusion and activation of these molecules at active sites.

Leg deflection was further analyzed using inhibitory and excitatory molecules, 50 μM curare and 400 μM L-glutamic acid, respectively. The deflection trace shows that curare weakened muscle

contraction, whereas L-glutamic acid induced significantly stronger deflection compared with the initial state (Fig. 3I). Statistical analysis of muscle contraction forces revealed that L-glutamic acid resulted in the strongest deflection ($N = 71$; $230.5 \pm 26.3 \mu\text{N}$) compared with the initial state ($N = 38$; $135.1 \pm 48.9 \mu\text{N}$) and curare treatment ($N = 44$; $83.8 \pm 27.5 \mu\text{N}$) (means \pm SD; $***P < 0.001$) (Fig. 3J). On the basis of this observation, we confirmed that muscle contraction observed in the NMJ crawler was primarily driven by NMJ signaling mechanisms via neurotransmitter transduction. Because curare binding is reversible, optical stimulation of the optogenetic neurospheres was able to restore the twitching of the muscle (movie S6), further validating the optogenetic function of the NMJ.

Optogenetic control of neuromuscular actuations

Although chemical stimulation exhibited promising results for regulating actuation modes of skeletal muscle, its controllability remains limited. To achieve the fine-tuning of the dynamics, we investigated how optostimulation of optogenetic motor neurons affects the twitching modes of the skeletal muscle. Previous studies have demonstrated that optostimulation can actively trigger both optogenetic neuronal firing (20, 29) and skeletal muscle contraction (6, 7, 13). However, it is known that there is a time delay between neuronal firing and actual muscle contraction (53), so a comprehensive investigation is necessary to understand this correlation.

For the experiment, we seeded neurospheres into only one chamber of the scaffold to avoid potential interference from independent signaling from the other NT. This produced a modified single-NT crawler. Optostimulation was conducted using an optical fiber emitting 450-nm wavelength light. We focused on two types of mechanical behaviors, twitching and crawling, depending on the orientation or position of the crawler (Fig. 4A). After preparing the modified NMJ crawler, we observed autonomous muscle contraction, but it was not strong enough to induce visible movement. The crawler showed slow locomotion after being stimulated with a 2-Hz pulsed light (Fig. 4B). Given that calcium imaging revealed that spontaneous neuronal firing patterns randomly occurred, the specific frequency of optostimulation likely caused synchronized neuronal firing, resulting in stronger net muscle contraction. The average velocity of the light-initiated crawling was 0.51 mm/min, with a maximum of 0.79 mm/min (Fig. 4C). After confirming the crawling behavior, we flipped the robot upside down to observe leg deflection by eliminating the frictional effects. First, we analyzed how both legs moved under the 2-Hz pulsed light (Fig. 4D). Despite the neurospheres being seeded on one side, both legs twitched in a highly synchronized manner, with a correlation factor of 0.86. This demonstrates that localized stimulation of motor units can drive contraction of the entire muscle, consistent with previous observations of optogenetic skeletal muscle contractions stimulated by an optical fiber (13).

Muscle twitching was further analyzed in a continuous recording by repeating the stimulation with 2- and 4-Hz pulsed light. The recording was analyzed in sections as indicated in Fig. 4E. Initially, we observed the natural twitching pattern of the muscle before stimulation

(Fig. 4E-i). Subsequently, 2-Hz pulsed light was applied for 1 min (Fig. 4E-ii), followed by a 40-s period without stimulation (Fig. 4E-iii). The stimulation was then repeated (Fig. 4E-iv), with a 5-min resting period in sequence (Fig. 4E-v_{a-c}). Afterward, the frequency of the light was changed to 4 Hz with a 30-s duration (Fig. 4E-vi, viii, and x), each followed by a resting period (Fig. 4E-vii, ix, and xi). After the measurements, we magnified each section to observe the twitching modes (Fig. 4F and fig. S8). As expected, muscle contraction occurred with random patterns and amplitudes before stimulation. When neurons were stimulated with 2-Hz pulsed light, the

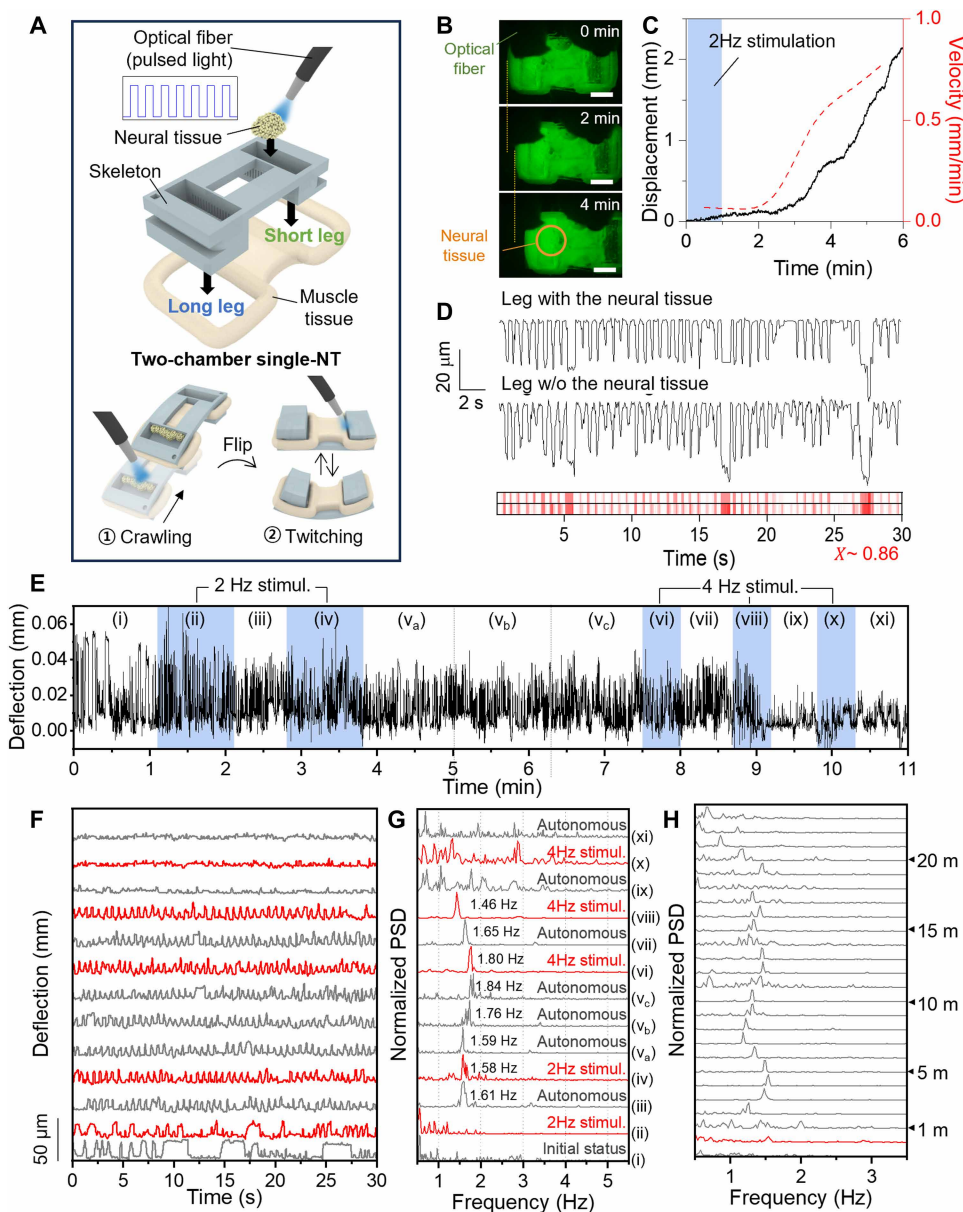


Fig. 4. Optogenetic response of single-NT NMJ crawler controlled by an optical fiber. (A) Illustration of the experimental setup consisting of single NT with an optical fiber. (B) Snapshots of the NMJ crawler and acceleration of crawling behavior by using 2-Hz optical stimulation (scale bars, 3 mm). (C) Crawling trajectory of the crawler over time. (D) Synchronized twitching of both legs under stimulation. (E) Observation of long leg twitching under 2- and 4-Hz frequencies of optical stimulation. (F) Representative deflection traces obtained from each section in (E). (G) PSDs of muscle twitching modes with respect to stimulus conditions. (H) Power densities obtained from continuous recording of muscle twitching after the 2-Hz stimulation.

twitching mode of the muscle gradually shifted to exhibit periodic patterns. The periodic patterns were maintained for several minutes even after the light source was turned off. Under 4-Hz stimulation, the twitching did not change immediately but eventually transitioned into a faster vibrational mode with lower amplitude as stimulation was repeated. These results suggest that neuronal activity modulation is closely related to muscle contraction behavior through synaptic signaling via the junction between motor neurons and myotubes (fig. S9). Specifically, before neuronal stimulation, contractions lasting longer than 2 s were observed, but such modes were no longer present after optostimulation. The initial twitching state of the muscle had a contraction duration of 0.43 ± 0.56 s ($N = 83$), slightly longer than that of the tissues stimulated with 2- and 4-Hz pulses, which were 0.31 ± 0.17 s ($N = 99$) and 0.35 ± 0.13 s ($N = 100$), respectively. Regarding deflection, noticeable differences were found, with values of 0.032 ± 0.023 mm for the prestimulation tissue, 0.038 ± 0.013 mm for 2-Hz stimulated tissue, and 0.013 ± 0.0059 mm for 4-Hz stimulated tissue. Although the average deflection of initial status was smaller than that during 2-Hz stimulation, it exhibited large variation among individual contractions. For the optostimulated samples, the 4-Hz exposure condition produced a significantly lower deflection than the 2-Hz condition, suggesting that there was insufficient time for the muscles to relax from contracted status. This observation is consistent with our previous results on skeletal muscle biohybrid crawlers with electrical and optical stimulation (7, 11).

Temporary tuning of neuromuscular actuation

For the numerical analysis of the twitching modes, each section of the trace was converted into PSD. Each spectrum was normalized to the maximum value and expressed in Fig. 4G. In the spectrum of Fig. 4G-i, no noticeable peaks were observed because of the random firing activity of neurons. However, when the tissue was exposed to 2-Hz pulsed light, some peaks began to appear in the range of 1 to 2 Hz. These peaks centered around 1.6 Hz and persisted even after the stimulation was turned off and repeated stimulation. The peak position remained between 1.59 and 1.84 Hz for more than 5 min as represented in Fig. 4G- v_{a-c} . In the case of 4-Hz stimulation, there was a gradual downshift of the peak position from 1.8 Hz to a lower value, as shown in Fig. 4G-vi to viii. After all signals disappeared from the 1.5- to 1.8-Hz range, a small peak emerged around 3 Hz, presumably in response to the stimulation with 4-Hz pulses. However, the amplitude of deflection was smaller than that measured under 2-Hz stimulation, making it challenging to obtain clear signals. As shown in the PSD data, we noticed that the actual mechanical twitching frequency was slightly lower than that of the optical stimulation, which could be explained by the time required to induce muscle contraction from the neuronal firing (54). We also observed a secondary peak that appeared at the doublet frequency of the highest peak. Doublet peaks are commonly seen in mechanical oscillating systems, which confirm the mechanical properties of the biological actuation of skeletal muscle and scaffold. Last, we observed sustainability of muscle contraction after being modulated by optostimulation (Fig. 4H). We applied a 2-Hz frequency of stimulation to the sample and recorded the twitching motion until it ceased. With the traces, we show the power density spectrum with a 1-min interval. According to the plot, twitching occurred within the ~1.3- to 1.7-Hz frequency range for 20 min, consistent with the twitching frequency of tuned muscle observed in Fig. 4G.

Wireless controlled optoelectronics integration

The results described above and shown in Fig. 4 characterize the mechanical output of an NMJ crawler in response to optostimulation using an immobilized optical fiber platform. To investigate the dynamic performance of a motile crawler, we integrated a wireless, battery-free optoelectronic device into the NMJ crawler scaffold. For this approach, we modified the scaffold design of the single-NT system to carry the optoelectronic device (Fig. 5A). The optoelectronic device was placed on the top surface of the crawler scaffold, secured in place with a stopper structure. Figure 5B presents an exploded view of the optoelectronic device, illustrating its layered structure. The device comprises a parylene-C encapsulation layer, an electronic components layer, and a two-layer flexible printed circuit board (PCB). The power-harvesting antenna, tuned to the 13.56-MHz near-field communication (NFC) frequency, featured a dual-sided circular coil (5.4 mm in diameter, 22 turns, 50- μ m trace width, and 50- μ m interspace) to enable radio frequency (RF) power conversion through resonant magnetic inductive coupling from an experimental container wired with a double-loop primary transmitting antenna. Harvested power drove five μ LEDs emitting 460-nm wavelength light, with frequency and pulse width controlled via software (figs. S10 and S11).

After preparing the modified optoelectronic NMJ crawlers, we evaluated their autonomous crawling as direct evidence of intact NMJ functionality. In the same batch, an NMJ crawler and a muscle-only control group were placed on a flat dish, and their motility was recorded over time (Fig. 5C). The results showed that the NMJ crawler exhibited strong dynamic locomotion, whereas the muscle-only control group remained quiescent, demonstrating that NMJ functions were properly established in the modified design. Furthermore, although the NMJ crawler showed locomotion regardless of optical stimulation, the nonoptogenetic muscle-only sample did not respond at all, as expected. We then optimized the number of neural cells in the NT (Fig. 5D). Unlike the two-chamber skeleton, the modified design had no compartmentalized chamber for the NT, allowing neurons to form more widespread junctions in the vicinity of the muscle tissue. We prepared 15 NMJ crawlers with three different numbers of neural cells (0.2, 0.8, and 2 M) in the extracellular matrix (ECM; volume ≈ 26 μ l) and compared their autonomous crawling velocities. The results showed no significant difference in crawling velocity but differences in the yield and performance of the devices. In the 0.2-M/26- μ l samples, as neurospheres were injected, 20% of the samples did not show any crawling behavior, likely because of the absence of NMJ formation due to too few neurons. In the 2-M/26- μ l samples, 40% of the samples did not move, possibly because of the highly active metabolism of neurons, which weakened the performances of myotubes around the neuronal tissue. In this experiment, the 0.8-M/26- μ l samples had 100% of the crawlers (five of five) showing autonomous crawling, whereas the 0.2-M/26- μ l and 2-M/26- μ l cells showed a lower yield. This suggests that the number of neurospheres in the tissue (and hence the original cell number used) is important for improved functional performance. We analyzed neurosphere aggregate sizes as a function of the cell numbers seeded. Neurospheres were found to individually be attached to muscle tissue for the 0.2-M/26- μ l sample, each smaller than 200 μ m in diameter. Increasing the density to 0.8-M/26- μ l cells resulted in aggregates of two or three neurospheres, ~300 to 400 μ m in diameter. At 2-M/26- μ l cells, aggregates were found to be larger, 1 mm in diameter (Fig. 5D-i and fig. S12). It is likely that the lower

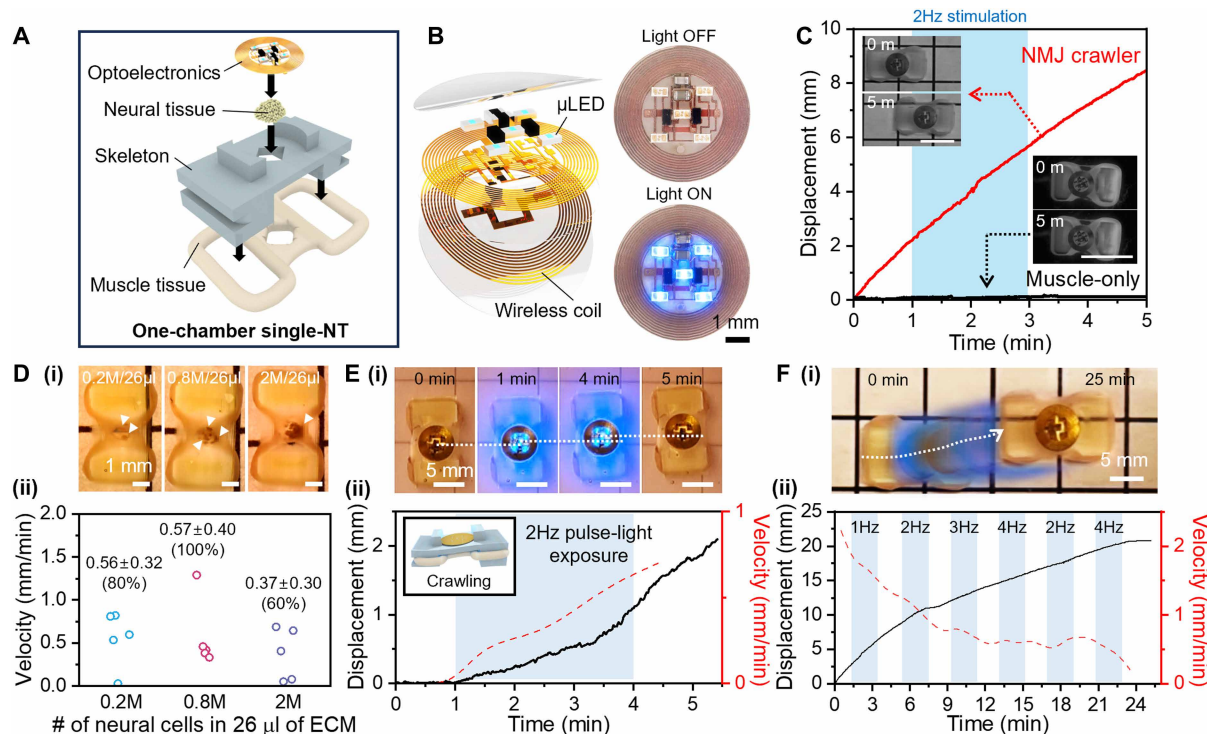


Fig. 5. Optogenetic control of single-NT NMJ crawler with onboard electronics. (A) Structure of the one-chamber, single-NT NMJ crawler with onboard optoelectronics. (B) Images of the optoelectronics composed of a power-harvesting antenna with five μ LEDs (fig. S10). (C) Comparison of crawling behaviors between nonoptogenetic pristine muscle and NMJ crawlers. Insets show the location of the crawlers after 5 min. Scale bars, 1 cm. (D) Optimization of the number of neural cells via measuring autonomous crawling of NMJ crawlers. (i) Optical images with different numbers of spheroids in the NT (scale bars, 1 mm) and (ii) the average velocities of autonomously crawling robots, both as a function of cell seeding density. (E) A case study of an optoelectronics-driven NMJ crawler that did not crawl before stimulation but showed boosted crawling after stimulation. (i) Images of the crawler for 5 min (scale bars, 5 mm). (ii) Recorded traces and velocity of the robot during the measurement. (F) A crawler showing high speed of autonomous crawling before stimulation but reduced its velocity after stimulation. (i) Actual displacement of the robot for 25 min. Scale bar, 5 mm. (ii) Measured traces and velocities under various stimulation conditions from 1 to 4 Hz.

number of spheroids in the NT does not result in enough functional NMJs for the muscle tissue to actuate. This is consistent with prior results where lower numbers of neurites and shorter neurite lengths were observed at both low and very high seeding densities (14), although those results were from individual neurospheres. A larger number of cells could also require greater nutritional contents for their metabolism, limiting diffusion of nutrients and oxygen, forming localized nutrient-deficient regions at the center of the NT (fig. S12) (55). Locally concentrated metabolic by-products such as lactate also negatively affect metabolic activities in peripheral cells (56). These factors could result in delayed cell differentiation or reduced cell viability within the reported protocols.

Next, we measured the unidirectional locomotion of the NMJ crawlers with optostimulation through onboard electronics. To determine the optostimulation conditions, we measured the minimum required stimulation time to modulate the twitching mode (fig. S13). Initial leg deflection was measured for 1 min without stimulation, followed by recording deflection under 2-Hz pulsed light exposure. The results showed that the twitching frequency changed quickly after the stimulation, within 1 min. Leveraging this finding, we ensured at least 1 min of stimulation to complete modulation of mechanical twitching. Therefore, we provided optical stimulation (1 min 20 s) to an NMJ crawler and confirmed that the crawler maintained its locomotion after turning off the stimulation (movie S7). This

coincides with our previous observation that the mechanical twitching can be temporarily tuned by modulated neuronal activity. Then, we analyzed changes in crawling characteristics depending on the optical stimulation. Figure 5E shows an example of a crawler that exhibited autonomous muscle contraction but not enough to induce crawling, as described in Fig. 4C. The crawler remained stationary until 2-Hz pulsed light was applied through the onboard electronics, at which point it began to crawl slowly toward the longer leg (movie S8). This could be explained by the synchronization of muscle contraction driven by ensemble neuronal firing evoked by the optical stimulation. Likewise, the crawler continued to move even after the stimulation was turned off, verifying the tuning of the mechanical actuation. In contrast, another crawler showed high-speed autonomous crawling even before stimulation but gradually slowed down under pulse-light exposure (Fig. 5F and movie S9). We varied the stimulation frequency from 1 to 4 Hz, followed by additional 2- and 4-Hz stimulation. In the experiment, each stimulation lasted for 2 min, followed by another 2 min when autonomous crawling occurred. As shown in the traces, the crawling velocity decreased under higher stimulation frequencies. When the pulsed light was set back to 2 Hz, the velocity seemed to increase slightly, but it remained slower than the initial 2-Hz conditioning, presumably because of muscular or neuronal fatigue after high-frequency stimulation. We examined the difference in velocities due to a single frequency of the stimulation,

2 or 4 Hz, to the same crawler and allowing for recovery time between the stimulation (fig. S14). Here, we observed that the crawler exhibited higher velocity at 2-Hz stimulation compared with that at 4-Hz stimulus condition, and these results are consistent with the data in Fig. 5F. To better understand this behavior, we observed the change in twitching mode under various stimulation conditions. The crawler was flipped upside down and stimulated by the electronics underneath it. Leg deflection was recorded with change of the pulse frequency (fig. S15 and movie S10). The result shows that the amplitude of leg deflection gradually declined under higher stimulation frequency. These results verify that the velocity of the crawler slowed as the stimulation frequency was increased. Additional FEA was also conducted, and the calculated active tension of the muscle was in agreement with the experimental data showing the gradual decrease in crawling velocity with the increase in stimulation frequency.

Although the simulated dynamic tendency coincided with experimental observation, there were some discrepancies in the range of velocities. We further conducted FEA simulation with extended variables to understand the crawling dynamics based on single- and dual-NT NMJ crawlers (fig. S16). According to the investigation, the discrepancies were likely caused by the model not accounting for all aspects of the experiments, such as nonuniform muscle thickness, varied friction after the crawler landed on the dish, and adaptation in neuronal firing with muscle contraction conditions. We also noticed that the overall motility of robots was slower in the single-NT system than the dual-NT one (fig. S17). In the single-NT model, the contraction intensity decreased with distance from the NT, potentially because of reduced neural activation. In contrast, the dual-NT crawler receives input from both NTs, resulting in more uniform contractions. It can also be postulated that the muscle tissue helps to synchronize the firing across the dual-NT system, a possibility that needs further study.

We also investigated the reproducibility of the NMJ functionality by comparing the optogenetic response across multiple biohybrid robots. In the single-NT NMJ crawler, we confirmed modulation of neuromuscular actuation and its persistence after stimulation (Fig. 6A). Achieving precise reproducible *in vitro* NMJ functionality in these biological robots remains challenging because of lengthy sample preparation processes, biological variability, uncontrollable cellular interactions, and other factors (2, 5, 9). In our experiments, autonomous twitching of NMJ crawlers was observed in most samples, but their synchronicity with the stimulation frequency varied across samples. To verify functional reproducibility, we collected PSDs from six samples that were stimulated and responded to 2-Hz stimulation for more

than 1 min and analyzed their responses (fig. S18). Twitching before stimulation occurred randomly, without specific patterns. After 2-Hz stimulation, most samples exhibited altered behavior compared with initial twitching, centering around 1.5 to 2.2 Hz. These samples generally maintained their twitching modes after stimulation stopped, with only a slight shift. These results indicate that optogenetic control of neuromuscular actuation is reproducible across multiple samples.

To evaluate the long-term performance of the NMJ crawler, we monitored response to stimulation and muscle contraction force daily under a 2-Hz optical stimulation regimen. Although cellular metabolism naturally releases proteolytic enzymes that aid in tissue remodeling *in vivo*, these enzymes can degrade *in vitro* biohybrid systems over time by degrading fibrin (57). Therefore, we investigated the stability of the NMJ functionalities over time. As shown in Fig. 6 (B and C), the crawler exhibited response to the stimulation and modulated twitching even after a week. Although the twitching frequencies varied slightly depending on the measurement days, autonomous twitching mode remained responsive to 2-Hz stimulation up to coculture day 17, showing their shifts in PSD mostly between 1.5 and 2.5 Hz (fig. S19). However, modulation became ambiguous thereafter. Despite the sustained modulation, the amplitude of contraction force gradually declined, likely because of accumulated stress and the release of cytotoxic metabolic by-products (Fig. 6D).

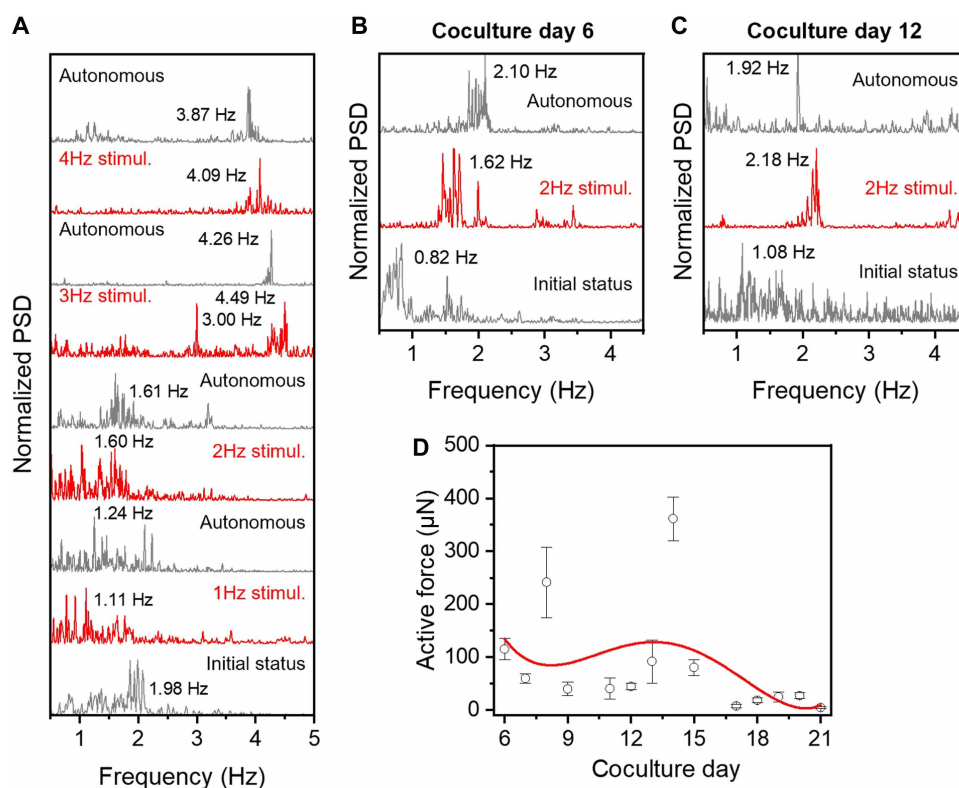


Fig. 6. Modulating neuromuscular actuation of the biohybrid crawler across samples and across time. (A) Representative example of altering muscular actuation depending on neurostimulation frequency (1 to 4 Hz). Long-term performance of an NMJ crawler was verified by measuring the mechanical responses of the robot for 21 days. The mechanical output to 2-Hz optical stimulation was converted to normalized PSDs, and data for 2 days are shown at (B) coculture day 6 and (C) coculture day 12. (D) Measured muscle contraction force in these long-term measurement experiments of an NMJ biohybrid crawler showing functionality lasting more than 2 weeks. Data represent means \pm SD ($N > 25$ independent actuation events).

Further studies are warranted to establish the specific reasons behind this loss of function after 17 days. Visible twitching persisted until coculture day 21, after which no mechanical output was observed. In comparison with our previous study on optogenetic muscle with the enzyme-inhibiting molecule ACA, which showed an average life span of 8.2 ± 0.5 days and 17 ± 3.9 days for 0× and 1× ACA (1 mg/ml), respectively, the NMJ crawler demonstrated a life span of 26 days (including 5 days of muscle differentiation and 21 days of coculture), representing an increased life expectancy even without ACA supplementation during coculture.

DISCUSSION

In this study, we investigated neuromodulation and the subsequent muscular actuation through NMJ signaling, aiming to establish a foundation for tunable neuromuscular biohybrid systems. Compared with our previous muscle-powered crawler/walker (6), this work introduces several neuron-muscle interfacial designs and contributions. First, we developed NMJ models using optogenetic neurospheres and pristine C2C12 myotubes and enabled selective stimulation of the neuronal component. Given the total number of functional biohybrid robots of varying designs demonstrated in this study, our assay protocols provide a robust platform for the reproducible creation of NMJ models. Second, we constructed 3D, untethered NMJ tissues using optimized mechanical and physical designs and experimental protocols. We explored two distinct designs for biohybrid crawlers: single- and dual-NT models. In the single-NT mode, for example, through-holes formed at the center of muscle strips were filled with partially coagulated ECM mixed with neurospheres, ensuring close proximity and stable integration between neurons and associated neurites and muscle tissue. Third, FEA simulations provided detailed insights into the respective mechanical actuation mechanisms, highlighting the role of neural placement and muscle morphology in motion dynamics. Last, by applying specific frequencies of optical stimulation, we were able to modulate the neuronal activity and the resulting muscle contractions.

Despite our reports, several challenges remain in achieving more precise control and tuning. Observed limitations included autonomous twitching from spontaneous neural firing, delayed neuromuscular response relative to stimulation input, and nonuniform actuations. These issues may arise from the fixed medium formulation, natural neuronal adaptation mechanisms (e.g., minimizing internal free energy), variability in neurotransmitter release, and sensitivity to experimental conditions. Although some variability can be reduced by optimizing medium formulations and using a well-controlled measurement setup, the inherent variability and complexity of neuronal systems could limit precision in control. In this study, we focused on leveraging the spontaneous properties of neural activity and showing evidence of modulation of function rather than achieving specific or precise control. This study provides a valuable platform for understanding and using adaptive neuromuscular dynamics by leveraging the emergent behaviors of neurons and NMJs.

In our study, the dynamic behavior of the NMJ crawlers could be categorized into two modes: initiation by optical stimulation or regulation by optical stimulation. These variations were likely influenced by local differences in myotube density, differentiation, orientation, and connectivity and the extent of NMJ formation, among others. Immunostaining of single-NT models revealed random myotube orientation around NMJ sites, which was a result of

the self-organization process through the physical slit where the NT is introduced. Changes in this through-hole size and myotube alignment during coculture could contribute to sample-to-sample variability. Further investigation will be required to accomplish further control, keeping in mind that biological emergence and self-organization are key aspects of these and all living systems. Nonetheless, most samples exhibited spontaneous twitching, confirming that autonomous neuromuscular activity is a common feature in our systems.

As future applications, these NMJ-based biohybrid robotics can be extended to include more sophisticated neural architecture with variable muscular structures. Although this study focused on simple modulation of neuromuscular activity with unidirectional locomotion by repetitive patterned stimulation, future systems could be bipedal systems that incorporate neural modules capable of self-regulation, such as central pattern generators (CPGs) or sensory-motor feedback loops to create bidirectional motion. Previous demonstrations of neuronal training for gameplay mimicry suggest that optogenetic stimulation can be used to enable adaptive responses and learning behavior in biohybrid robots (23). Furthermore, to realize a biorobot that could move in multiple directions, a design where a single- or multiple-NT system controls different independent muscles will have to be realized and is the subject of our future reports.

In addition to robotics, this platform offers promise for biomedical applications. Our findings provide a baseline for how healthy NMJs respond to stimulation. This knowledge can be translated into disease modeling by incorporating cells from patients with neurodegenerative or muscular disorders. Drug screening and therapeutic treatment could be evaluated on the basis of functional restoration in mechanical output. Furthermore, immune responses and inflammation could be studied through chemical induction, with released cytokines serving as readouts. These applications highlight the broader potential of neuromuscular actuation as a functional biomarker in both biohybrid engineering and disease research.

In summary, we successfully developed an optogenetically controlled NMJ biohybrid soft robot integrated with optoelectronics, enabling autonomous movement driven by spontaneous neural firing. The NMJ crawler exhibited reliably modulated muscle actuation through optostimulation, with FEA simulations and dynamic mechanical measurements validating its unidirectional crawling behavior. We further demonstrated that optostimulation not only synchronized neuronal firing but also resulted in sustained muscle contraction, revealing temporarily tuned mechanical outputs that persisted after turning off the stimulation. By modulating stimulation frequencies, we observed alteration in both crawling velocity and muscle twitching modes. On the basis of PSD analysis, we confirmed that the frequency of muscle twitching was guided by the input stimulation. These findings provide valuable insights into the correlation between neuronal signaling and muscle actuation, underpinning the development of tunable biohybrid systems with potential applications in soft robotics, neuronal tuning, and medical devices.

MATERIALS AND METHODS

Fabrications of 3D-printed hydrogel scaffolds

After designing hydrogel scaffolds using SolidWorks or Rhinoceros (figs. S1 and S2), we 3D-printed the structures with a digital light 3D printer (PICO2, Asiga). For the printing resin, 20% (v/v) PEGDA

($M_n = 700$ g/mol; Sigma-Aldrich) was prepared in distilled water. To cross-link monomers, we added a photoinitiator, lithium phenyl-2,4,6-trimethylbenzoylphosphinate (1 mg/ml; Sigma-Aldrich), to the 20% PEGDA solution. To minimize light scattering, we mixed sunset yellow dye (0.6 mg/ml; Sigma-Aldrich) into the solution. Printed scaffolds were immersed in 10% (v/v) bleach for 30 min to remove the dye. They were then sterilized in 70% (v/v) isopropyl alcohol (IPA) overnight and stored in phosphate-buffered saline (PBS) at 4°C. PBS was replaced every other day to rinse off residual bleach and IPA.

Preparation of the NMJ tissue

The timeline of tissue preparation is described in Fig. 1B. Briefly, C2C12 skeletal myoblasts were cultured in the GM consisting of high-glucose Dulbecco's modified Eagle's medium (DMEM), 10% (v/v) fetal bovine serum (FBS), 1% (v/v) penicillin/streptomycin, and 1% (v/v) GlutaMAX. Medium was changed every other day until cells reached ~70% confluency. Then, cells were harvested using TrypLE express enzyme and resuspended in the fresh GM. Myoblasts ($\approx 1.5 \times 10^6$ cells) were mixed with ECM solution consisting of 115 μ l of GM⁺ [GM supplemented with 2% ACA, 6 μ l of thrombin (100 U/ml), 90 μ l of Matrigel, and 75 μ l of fibrinogen (16 mg/ml)]. The cell-gel solution was gently mixed with pipetting and seeded into the hydrogel mold. After incubation at 37°C for 2 hours, a sample container was filled with fresh GM⁺. After 3 days of cell proliferation and tissue compaction, samples were switched to the DM consisting of high-glucose DMEM, 10% (v/v) heat-inactivated horse serum (HIHS), 1% (v/v) penicillin/streptomycin, 1% (v/v) GlutaMAX supplemented with 2% (v/v) ACA, and 0.005% (v/v) insulin-like growth factor 1 (IGF-1) (DM⁺⁺). The muscle tissues were differentiated for 5 days with medium changes every other day.

A mouse embryonic fibroblast (MEF) feeder layer was prepared in a medium containing the components listed in table S1 to expand mESCs. After culturing the MEFs for 2 days, the mESCs were cultured on the MEF layer with a medium composed of the ingredients listed in table S2. Before the stem cell colonies contacted each other, they were selectively collected by trypsinizing all cells and removing the MEFs by preplating on a gelatin-coated flask. The stem cells were then induced into neuronal stem cells (NSCs) by being cultured in induction medium (table S3) for 2 days, supplemented with noggin, fibroblast growth factor 8 (FGF-8), and basic fibroblast growth factor (bFGF). After this, the NSCs were further differentiated into motor neurons in the DM (table S4) for 3 days and maintained in the maintenance medium (table S5) for an additional 2 days. Neurospheres became visible during this process as the neural cells aggregated into spheroids. After completing neuronal maintenance, the neurospheres were collected and resuspended in the coculture medium (table S6) containing 8×10^5 cells. After medium aspiration, these neurospheres were gently mixed with ECM, 0.5 μ l of thrombin (100 U/ml), 8.1 μ l of Matrigel, 6.75 μ l of fibrinogen (16 mg/ml), and 10.75 μ l of the coculture medium (total volume ≈ 26 μ l). After allowing the mixture to settle at room temperature for 5 min, the partially gelled cell-matrix mixture was seeded adjacent to the muscle tissue.

Optogenetic stimulation of neurospheres

Optical stimulation was performed via either an LED module driver (465-nm wavelength) with an optical fiber (Doric Lenses) or fabricated optoelectronics with five μ LEDs (460-nm wavelength). All crawling data and force data were recorded using a portable digital microscope (Dino-Lite). Frequency, pulse duration, and power of

the light were controlled by Doric or NeuroLux software. Frequency of the light varied from 1 to 4 Hz, maintaining its pulse duration at 100 ms.

Immunostaining process

Immunohistochemistry imaging was conducted to observe protein expression and localization in neuromuscular tissue. The tissue was carefully separated from the hydrogel skeleton and fixed using 4% PFA for 20 min. It was then immersed in 1% bovine serum albumin (BSA) and 0.25% Triton-X in PBS for 2 hours to permeabilize the cell membrane and block nonspecific binding sites. To label myotubes, neurons, nuclei, and AChRs, we incubated the tissue overnight with antibodies in 1% BSA containing myosin 4 monoclonal antibody (MF-20) conjugated with Alexa Fluor 488 nm (1:250), Tuj1 (1:250), and α -BTX conjugated with Alexa Fluor 647 dye (1:250). After rinsing the tissue with PBS three times, the tissue was further incubated with fluorescent tags, including Alexa Fluor 568 nm (anti-rabbit, 1:500) and DAPI (1:5000), for 2 hours before imaging.

RNA extraction and purification

For analyzing the genetic regulation of neuromuscular tissues, RNA was extracted from the prepared tissues using an RNeasy Mini Kit (Qiagen). Living tissues were snap-frozen in liquid nitrogen, followed by lysis using TRIzol with homogenization. After adding chloroform, the sample was incubated in ice for 15 min. RNA was selectively collected by transferring the aqueous phase of the solution after centrifugation at 12,000 rpm for 15 min at 4°C. After several rinsing steps in a spin column, high-quality RNA was obtained through elution. The qPCR and RNA sequencing details are described in Supplementary Methods.

Fabrication of wireless optoelectronic devices

The device was constructed on a custom-made two-layer flexible PCB composed of copper (18 μ m):polyethylene terephthalate (25 μ m):copper (18 μ m). Circuit component assembly was performed using low-temperature soldering with the tin-bismuth-silver alloy solder paste (ChipQuik Sn₄₂/Bi_{57.6}/Ag_{0.4}). After soldering, the devices were encapsulated in a 10- μ m parylene-C layer via chemical vapor deposition (CVD; Special Coating Systems), providing waterproofing, durability, and biocompatibility.

Experimental implementation for wireless communication

The Power Distribution and Control (PDC) box, paired with an RF impedance matching tuner, enabled efficient wireless power delivery through a custom-shaped double-loop antenna resonant at 13.56 MHz. Software interfacing through USB with the PDC box controlled the operational parameters of the optoelectronic devices. The internal RF switch of the PDC box generated precisely modulated operational pulses (e.g., 2-Hz frequency, 10-ms pulse width, and 2% duty cycle) to control the optoelectronic devices within the experimental container.

FEA of the NMJ crawler

The commercial finite element software Abaqus (Dassault Systems, version 2023) was used for the characterization of muscle tissue and the simulation of crawling locomotion. The 3D scaffold and muscle were modeled by solid elements (C3D8RH elements), the circuit board was modeled by shell elements (S4R elements), and the substrate was modeled as a rigid plane. The crawlers were fully submerged in

physiological solution, so gravitational and buoyant forces were applied to their bodies. The hydrodynamic force during locomotion was approximated using a damping force applied on the crawler. The contact and friction force between the crawler and the substrate were considered by using the isotropic Coulomb friction model. The detailed methodology and material parameters are given in Supplementary Methods and tables S7 and S8.

Statistical analysis

Individual data points were collected and analyzed using Origin 2022 software (OriginLab Corporation, Northampton, MA, USA) and are presented as means \pm SD. Student's *t* test was applied to compare the means of two groups using either paired or two-sample *t* test functions. *P* values were used to indicate statistical significance ($*P < 0.05$, $**P < 0.01$, and $***P < 0.001$).

Supplementary Materials

The PDF file includes:

Methods

Figs. S1 to S19

Tables S1 to S8

Other Supplementary Material for this manuscript includes the following:

Movies S1 to S10

MDAR Reproducibility Checklist

REFERENCES AND NOTES

- M. R. Picciotto, M. J. Higley, Y. S. Mineur, Acetylcholine as a neuromodulator: Cholinergic signaling shapes nervous system function and behavior. *Neuron* **76**, 116–129 (2012).
- O. Aydin, X. Zhang, S. Nuethong, G. J. Pagan-Diaz, R. Bashir, M. Gazzola, M. T. A. Saif, Neuromuscular actuation of biohybrid motile bots. *Proc. Natl. Acad. Sci. U.S.A.* **116**, 19841–19847 (2019).
- K. Y. Lee, S.-J. Park, D. G. Matthews, S. L. Kim, C. A. Marquez, J. F. Zimmerman, H. A. M. Ardoña, A. G. Kleber, G. V. Lauder, K. K. Parker, An autonomously swimming biohybrid fish designed with human cardiac biophysics. *Science* **375**, 639–647 (2022).
- S.-J. Park, M. Gazzola, K. S. Park, S. Park, V. Di Santo, E. L. Blevins, J. U. Lind, P. H. Campbell, S. Dauth, A. K. Capulli, Phototactic guidance of a tissue-engineered soft-robotic ray. *Science* **353**, 158–162 (2016).
- M. Shin, T. Ha, J. Lim, J. An, G. Beak, J. H. Choi, A. A. Melvin, J. Yoon, J. W. Choi, Human motor system-based biohybrid robot-on-a-chip for drug evaluation of neurodegenerative disease. *Adv. Sci.* **11**, 2305371 (2024).
- Y. Kim, Y. Yang, X. Zhang, Z. Li, A. Vázquez-Guardado, I. Park, J. Wang, A. I. Efimov, Z. Dou, Y. Wang, Remote control of muscle-driven miniature robots with battery-free wireless optoelectronics. *Sci. Robot.* **8**, ead1053 (2023).
- R. Raman, C. Cvetkovic, S. G. Uzel, R. J. Platt, P. Sengupta, R. D. Kamm, R. Bashir, Optogenetic skeletal muscle-powered adaptive biological machines. *Proc. Natl. Acad. Sci. U.S.A.* **113**, 3497–3502 (2016).
- R. Kinjo, Y. Morimoto, B. Jo, S. Takeuchi, Biohybrid bipedal robot powered by skeletal muscle tissue. *Matter* **7**, 948–962 (2024).
- H. Tetsuka, S. Gobbi, T. Hatanaka, L. Pirrami, S. R. Shin, Wirelessly steerable bioelectronic neuromuscular robots adapting neurocardiac junctions. *Sci. Robot.* **9**, eado0051 (2024).
- Y. Morimoto, H. Onoe, S. Takeuchi, Biohybrid robot powered by an antagonistic pair of skeletal muscle tissues. *Sci. Robot.* **3**, eaat4440 (2018).
- C. Cvetkovic, R. Raman, V. Chan, B. J. Williams, M. Tolish, P. Bajaj, M. S. Sakar, H. H. Asada, M. T. A. Saif, R. Bashir, Three-dimensionally printed biological machines powered by skeletal muscle. *Proc. Natl. Acad. Sci. U.S.A.* **111**, 10125–10130 (2014).
- G. J. Pagan-Diaz, X. Zhang, L. Grant, Y. Kim, O. Aydin, C. Cvetkovic, E. Ko, E. Solomon, J. Hollis, H. Kong, T. Saif, M. Gazzola, R. Bashir, Simulation and fabrication of stronger, larger, and faster walking biohybrid machines. *Adv. Funct. Mater.* **28**, 1801145 (2018).
- J. Wang, Y. Wang, Y. Kim, T. Yu, R. Bashir, Multi-actuator light-controlled biological robots. *APL Bioeng.* **6**, 036103 (2022).
- C. Cvetkovic, M. H. Rich, R. Raman, H. Kong, R. Bashir, A 3D-printed platform for modular neuromuscular motor units. *Microsyst. Nanoeng.* **3**, 17015 (2017).
- T. Osaki, S. G. Uzel, R. D. Kamm, Microphysiological 3D model of amyotrophic lateral sclerosis (ALS) from human iPSC-derived muscle cells and optogenetic motor neurons. *Sci. Adv.* **4**, eaat5847 (2018).
- G. Nagel, T. Szellas, W. Huhn, S. Kateriya, N. Adeishvili, P. Berthold, D. Ollig, P. Hegemann, E. Bamberg, Channelrhodopsin-2, a directly light-gated cation-selective membrane channel. *Proc. Natl. Acad. Sci. U.S.A.* **100**, 13940–13945 (2003).
- H. Watanabe, H. Sano, S. Chiken, K. Kobayashi, Y. Fukata, M. Fukata, H. Mushiaka, A. Nambu, Forelimb movements evoked by optogenetic stimulation of the macaque motor cortex. *Nat. Commun.* **11**, 3253 (2020).
- J. B. Bryson, C. B. Machado, M. Crossley, D. Stevenson, V. Bros-Facer, J. Burrone, L. Greensmith, I. Lieberam, Optical control of muscle function by transplantation of stem cell-derived motor neurons in mice. *Science* **344**, 94–97 (2014).
- J. Li, Y. Liu, L. Yuan, B. Zhang, E. S. Bishop, K. Wang, J. Tang, Y.-Q. Zheng, W. Xu, S. Niu, A tissue-like neurotransmitter sensor for the brain and gut. *Nature* **606**, 94–101 (2022).
- G. J. Pagan-Diaz, K. P. Ramos-Cruz, R. Sam, M. E. Kandel, O. Aydin, M. T. A. Saif, G. Popescu, R. Bashir, Engineering geometrical 3-dimensional untethered in vitro neural tissue mimic. *Proc. Natl. Acad. Sci. U.S.A.* **116**, 25932–25940 (2019).
- G. J. Pagan-Diaz, E. Kilacarlan, M. Wester, S. Rahman, O. Aydin, L. Gapinske, Y. Kim, D. Buoros, M. S. A. Taher, R. Bashir, Engineering 3D neuronal networks with directional endogenous neuronal plasticity pathways. *bioRxiv* 2023.05.17.540876 [Preprint] (2023). <https://doi.org/10.1101/2023.05.17.540876>.
- M. Y. Cheng, E. H. Wang, W. J. Woodson, S. Wang, G. Sun, A. G. Lee, A. Arac, L. E. Fenno, K. Deisseroth, G. K. Steinberg, Optogenetic neuronal stimulation promotes functional recovery after stroke. *Proc. Natl. Acad. Sci. U.S.A.* **111**, 12913–12918 (2014).
- B. J. Kagan, A. C. Kitchin, N. T. Tran, F. Habibollahi, M. Khajehnejad, B. J. Parker, A. Bhat, B. Rollo, A. Razi, K. J. Friston, In vitro neurons learn and exhibit sentience when embodied in a simulated game-world. *Neuron* **110**, 3952–3969.e8 (2022).
- R. A. John, J. Acharya, C. Zhu, A. Surendran, S. K. Bose, A. Chaturvedi, N. Tiwari, Y. Gao, Y. He, K. K. Zhang, Optogenetics inspired transition metal dichalcogenide neuristors for in-memory deep recurrent neural networks. *Nat. Commun.* **11**, 3211 (2020).
- J. Wang, X. Zhang, J. Park, I. Park, E. Kilacarlan, Y. Kim, Z. Dou, R. Bashir, M. Gazzola, Computationally assisted design and selection of maneuverable biological walking machines. *Adv. Intell. Syst.* **3**, 2000237 (2021).
- H. Wichterle, I. Lieberam, J. A. Porter, T. M. Jessell, Directed differentiation of embryonic stem cells into motor neurons. *Cell* **110**, 385–397 (2002).
- H. Wichterle, M. Peljto, Differentiation of mouse embryonic stem cells to spinal motor neurons. *Curr. Protoc. Stem Cell Biol.* **5**, 1H.1.1–1H.1.9 (2008).
- C.-Y. Wu, D. Whye, R. W. Mason, W. Wang, Efficient differentiation of mouse embryonic stem cells into motor neurons. *J. Vis. Exp.* **2012**, 3813 (2012).
- S. G. Uzel, R. J. Platt, V. Subramanian, T. M. Pearl, C. J. Rowlands, V. Chan, L. A. Boyer, P. T. So, R. D. Kamm, Microfluidic device for the formation of optically excitable, three-dimensional, compartmentalized motor units. *Sci. Adv.* **2**, e1501429 (2016).
- A. J. Denzer, R. Brandenberger, M. Gesemann, M. Chiquet, M. A. Ruegg, Agrin binds to the nerve–muscle basal lamina via laminin. *J. Cell Biol.* **137**, 671–683 (1997).
- K.-Y. Huang, G. Upadhyay, Y. Ahn, M. Sakakura, G. J. Pagan-Diaz, Y. Cho, A. C. Weiss, C. Huang, J. W. Mitchell, J. Li, Neuronal innervation regulates the secretion of neurotrophic myokines and exosomes from skeletal muscle. *Proc. Natl. Acad. Sci. U.S.A.* **121**, e2313590121 (2024).
- F. Chen, L. Qian, Z.-H. Yang, Y. Huang, S. T. Ngo, N.-J. Ruan, J. Wang, C. Schneider, P. G. Noakes, Y.-Q. Ding, Rapsyn interaction with calpain stabilizes AChR clusters at the neuromuscular junction. *Neuron* **55**, 247–260 (2007).
- K. Okada, A. Inoue, M. Okada, Y. Murata, S. Kakuta, T. Jigami, S. Kubo, H. Shiraishi, K. Eguchi, M. Motomura, The muscle protein Doka-7 is essential for neuromuscular synaptogenesis. *Science* **312**, 1802–1805 (2006).
- H.-J. Garchon, F. Djabiri, J.-P. Viard, P. Gajdos, J.-F. Bach, Involvement of human muscle acetylcholine receptor alpha-subunit gene (CHRNA) in susceptibility to myasthenia gravis. *Proc. Natl. Acad. Sci. U.S.A.* **91**, 4668–4672 (1994).
- Z. G. Luo, Q. Wang, J. Z. Zhou, J. Wang, Z. Luo, M. Liu, X. He, A. Wynshaw-Boris, W. C. Xiong, B. Lu, Regulation of AChR clustering by Dishevelled interacting with MuSK and PAK1. *Neuron* **35**, 489–505 (2002).
- J. B. Jaynes, J. E. Johnson, J. N. Buskin, C. L. Gartside, S. D. Hauschka, The muscle creatine kinase gene is regulated by multiple upstream elements, including a muscle-specific enhancer. *Mol. Cell. Biol.* **8**, 62–70 (1988).
- D. C. Bowen, J. S. Park, S. Bodine, J. L. Stark, D. M. Valenzuela, T. N. Stitt, G. D. Yancopoulos, R. M. Lindsay, D. J. Glass, P. S. DiStefano, Localization and regulation of MuSK at the neuromuscular junction. *Dev. Biol.* **199**, 309–319 (1998).
- J. N. Waddell, P. Zhang, Y. Wen, S. K. Gupta, A. Yevtdiyenko, J. V. Schmidt, C. A. Bidwell, A. Kumar, S. Kuang, Dlk1 is necessary for proper skeletal muscle development and regeneration. *PLOS ONE* **5**, e15055 (2010).
- H. Zhou, T. Muramatsu, W. Halfter, K. W. Tsim, H. B. Peng, A role of midkine in the development of the neuromuscular junction. *Mol. Cell. Neurosci.* **10**, 56–70 (1997).
- F. Ferrero Restelli, P. A. Fontanet, A. P. De Vincenti, T. L. Falzone, F. Ledda, G. Paratcha, Tetraspanin1 promotes NGF signaling by controlling TrkA receptor proteostasis. *Cell. Mol. Life Sci.* **77**, 2217–2233 (2020).

41. V. Pongrakhananon, H. Saito, S. Hiver, T. Abe, G. Shioi, W. Meng, M. Takeichi, CAMSAP3 maintains neuronal polarity through regulation of microtubule stability. *Proc. Natl. Acad. Sci. U.S.A.* **115**, 9750–9755 (2018).
42. I. Becker, L. Wang-Eckhardt, J. Lodder-Gadaczek, Y. Wang, A. Grünewald, M. Eckhardt, Mice deficient in the NAAG synthetase II gene *Rimk1a* are impaired in a novel object recognition task. *J. Neurochem.* **157**, 2008–2023 (2021).
43. K. Yokoyama, T. Tezuka, M. Kotani, T. Nakazawa, N. Hoshina, Y. Shimoda, S. Kakuta, K. Sudo, K. Watanabe, Y. Iwakura, NYAP: A phosphoprotein family that links PI3K to WAVE1 signalling in neurons. *EMBO J.* **30**, 4739–4754 (2011).
44. A. H. Rasmussen, H. B. Rasmussen, A. Silahdaroglu, The DLGAP family: Neuronal expression, function and role in brain disorders. *Mol. Brain* **10**, 43 (2017).
45. K. Koles, V. Budnik, Wnt signaling in neuromuscular junction development. *Cold Spring Harb. Perspect. Biol.* **4**, a008045 (2012).
46. T. Hui, H. Jing, X. Lai, Neuromuscular junction-specific genes screening by deep RNA-seq analysis. *Cell Biosci.* **11**, 81 (2021).
47. T. C. Südhof, Neuroligins and neuroligins link synaptic function to cognitive disease. *Nature* **455**, 903–911 (2008).
48. A.-K. Lutz, S. Pfaender, B. Inceap, V. Ioannidis, I. Ottonelli, K. J. Föhr, J. Cammerer, M. Zoller, J. Higelin, F. Giona, Autism-associated SHANK3 mutations impair maturation of neuromuscular junctions and striated muscles. *Sci. Transl. Med.* **12**, eaaz3267 (2020).
49. J. Lee, J. T. Littleton, Transmembrane tethering of synaptotagmin to synaptic vesicles controls multiple modes of neurotransmitter release. *Proc. Natl. Acad. Sci. U.S.A.* **112**, 3793–3798 (2015).
50. M. Adler, R. E. Sheridan, S. S. Deshpande, G. A. Oyler, Neuromuscular transmission and muscle contractility in SNAP-25-deficient coloboma mice. *Neurotoxicology* **22**, 775–786 (2001).
51. S. Berto, N. Usui, G. Konopka, B. L. Fogel, ELAVL2-regulated transcriptional and splicing networks in human neurons link neurodevelopment and autism. *Hum. Mol. Genet.* **25**, 2451–2464 (2016).
52. M. Dittrich, A. E. Homan, S. D. Meriney, Presynaptic mechanisms controlling calcium-triggered transmitter release at the neuromuscular junction. *Curr. Opin. Physiol.* **4**, 15–24 (2018).
53. G. M. Van Acker III, C. W. Luchies, P. D. Cheney, Timing of cortico-muscle transmission during active movement. *Cereb. Cortex* **26**, 3335–3344 (2016).
54. V. Brezina, I. V. Orekhova, K. R. Weiss, The neuromuscular transform: The dynamic, nonlinear link between motor neuron firing patterns and muscle contraction in rhythmic behaviors. *J. Neurophysiol.* **83**, 207–231 (2000).
55. H. Zheng, S. W. Harcum, J. Pei, W. Xie, Stochastic biological system-of-systems modelling for iPSC culture. *Commun. Biol.* **7**, 39 (2024).
56. P. Gupta, K. Hourigan, S. Jadhav, J. Bellare, P. Verma, Effect of lactate and pH on mouse pluripotent stem cells: Importance of media analysis. *Biochem. Eng. J.* **118**, 25–33 (2017).
57. C. Cvetkovic, M. C. Ferrall-Fairbanks, E. Ko, L. Grant, H. Kong, M. O. Platt, R. Bashir, Investigating the life expectancy and proteolytic degradation of engineered skeletal muscle biological machines. *Sci. Rep.* **7**, 3775 (2017).

Acknowledgments: This research was conducted using facilities at the Holonyak Micro and Nanotechnology Laboratory. We appreciate R. Kamm from the Massachusetts Institute of Technology for providing transfected cell lines and Y. Vlasov from the University of Illinois at Urbana-Champaign for discussions on neuronal stimulation and activity. We also thank the staff at the Holonyak Micro and Nanotechnology Laboratory at University of Illinois at Urbana-Champaign. **Funding:** This work was funded by the National Science Foundation (Expeditions in Computing Grant 2123781 to T.A.S., J.A.R., and R.B.), National Institutes of Health (R61HL159948 to H.J.K.), and a Chan Zuckerberg Biohub Chicago Acceleration Research Award to R.B. **Author contributions:** Conceptualization and design: H.M., Y.W., J.W., W.K., J.Y., Y.K., and R.B. Electronic fabrications and characterizations: Y.W., Z.Z., J.G., X.L., and J.A.R. Biofabrication and analysis for the NMJ model: H.M., J.W., W.K., O.A., S.K., J.Y., J.L., K.W., Y.K., Y.X., T.R., H.J.K., T.A.S., and R.B. Computational modeling and design: Y.W., X.L., and Y.H. Writing: H.M., Y.W., J.W., X.L., O.A., S.K., H.J.K., T.A.S., Y.H., J.A.R., and R.B. **Competing interests:** The authors declare that they have no competing interests. **Data and materials availability:** All data needed to evaluate the conclusions in the paper are present in the paper and/or the Supplementary Materials. The data for this study have been deposited in the Dryad repository at DOI: 10.5061/dryad.pk0p2nh21.

Submitted 12 November 2024

Resubmitted 7 May 2025

Accepted 11 August 2025

Published 3 September 2025

10.1126/scirobotics.adu5830